

## Comparison of NCEP–NCAR Reanalysis with 1987 FIFE Data

ALAN K. BETTS

*Pittsford, Vermont*

SONG-YOU HONG AND HUA-LU PAN

*NCEP Environmental Modeling Center, Washington, D.C.*

(Manuscript received 17 July 1995, in final form 5 December 1995)

### ABSTRACT

Data from the FIFE experiment of the summer of 1987 are used to assess the diurnal and seasonal cycles of the surface energy budget and boundary layer in the NCEP–NCAR reanalysis, which used the summer 1995 version of the Medium-Range Forecast model. The seasonal agreement is quite good, reflecting the improvements in land-surface parameterizations in recent years. Detailed studies, however, identify several places where still further improvements in model parameterizations are possible. Clear-sky shortwave absorption and cloudiness may be underestimated in this model as has been noticed in other global models. More frequent updates of the model cloud cover (currently every 3 h) would improve the land-surface interaction after the initial onset of precipitation. The model produces a realistic well-mixed boundary layer, but underestimates boundary layer deepening by entrainment. For much of the summer, precipitation is close to that observed; however, for a period in June and early July, the reanalysis model has excess precipitation, which comes from daytime interactions between the surface evaporation, boundary layer, and convection schemes. The model, which has a deep 2-m soil reservoir, has adequate soil moisture storage for several weeks without rain, although surface evaporative fraction fluctuates more strongly after rain than is observed. Surface evaporation is generally too high at night, especially in high winds. This analysis suggests several improvements to the model parameterizations, some of which have already been implemented in the operational MRF model.

### 1. Introduction

The National Centers for Environmental Prediction [NCEP, formerly the National Meteorological Center (NMC)], and the National Center for Atmospheric Research (NCAR) have embarked on a reanalysis project that uses a frozen version of the current operational Medium-Range Forecast (MRF) analysis–forecast system at a triangular spectral truncation of T-62 with 28 levels in the vertical to perform data assimilation using past data from 1957 to 1996 (Kalnay and Jenne 1991; Kalnay et al. 1996). The European Centre for Medium-Range Weather Forecasts (ECMWF) is undertaking a similar reanalysis project (for a 15-yr time period) with a current version of their model, as is the Data Assimilation Office at the Goddard Laboratory for Atmospheres (for the time period starting in 1985; Schubert et al. 1993). The idea of a uniformly assimilated dataset is attractive and believed important for the study of climate and climate changes. Current archives of gridpoint data commonly used in climate

studies are derived from operational numerical weather prediction centers, and are the results of production data assimilation suites. As the centers upgrade their analysis or forecast procedures over the years, the character of the model analyses often change, as has been pointed out previously by many scientists. In studies of the climate change to date, researchers have had to deal with changes in the model data due both to real atmospheric changes and due to changes in assimilation procedures. For this reason, reanalysis projects were proposed some years ago (Bengtsson and Shukla 1988) to remove changes due to assimilation procedures as much as possible. It is only recently that these efforts are coming to fruition. Since the resulting analyses will be valuable to the scientific research community for years to come, it is useful to document the character of the data by comparison with actual observations, since the current analysis–forecast procedures are certainly not perfect. In this paper, we analyze the land-surface and boundary layer (BL) components of the NCEP–NCAR reanalysis system, and point out both the strengths and weaknesses apparent in the data.

We compare the surface meteorological parameters and surface energy budget from the closest grid point in the T-62 L28 NCEP–NCAR reanalysis (archived every 6 h) with average data from the 1987 First

---

*Corresponding author address:* Dr. Alan K. Betts, RR 3, Box 3125, Pittsfield, VT 05763.  
E-mail: betts@aol.com

ISLSCP (International Satellite Land Surface Climatology Project) Field Experiment (FIFE) site in the Konza prairie south of Manhattan, Kansas. We also explore how well short-term 24-h forecasts from the 1987 reanalysis, using the same version of the model at a higher T-126 resolution, reproduce the observed diurnal cycle for selected days. During FIFE, an extensive series of surface meteorological observations, radiosondes, and surface energy budget measurements were collected during the 1987 summer growing season (Sellers et al. 1992; Sellers and Hall 1992). The FIFE observations were made on a  $15 \text{ km} \times 15 \text{ km}$  site. Betts et al. (1993) averaged the surface meteorological and flux data to give a single time series representative of the FIFE site for the time period 24 May to 16 October 1987. They used this dataset to identify errors in the ECMWF land-surface and BL formulations (Betts et al. 1993); subsequently this and other datasets were used to develop improved parameterizations for that model (Viterbo and Beljaars 1995). This compacted FIFE time series has proved useful for other land-surface model development studies (Liang et al. 1994; Chen et al. 1996).

This paper compares this average FIFE time series with products from the nearest grid point of the MRF reanalysis model. The model representation of the diurnal and seasonal cycle is encouraging, although the data identify aspects of the model parameterizations that need further development. It is important to realize that we are using an average time series for a  $15 \text{ km} \times 15 \text{ km}$  domain in Kansas (centered near  $39^\circ\text{N}$ ,  $96.5^\circ\text{W}$ ) to identify systematic errors in a global model with a considerably larger effective grid resolution of order 100–200 km (depending on the spectral resolution). There are several reasons why the comparison is meaningful. For the summer of 1987, conditions over the FIFE grassland site were relatively homogeneous, so that simple averaging of the data gave a representative mean. The disparity of scale is partly offset by the fact that the diurnal cycle over land averages over considerable advection distances (again of order 100–200 km). Over the central United States, the rawinsonde network is sufficiently dense to define the synoptic-scale fields down to the resolution of the global model. On this scale the fields are smoothly varying, so that if we had used an adjacent grid point from the global model, we would have reached similar conclusions about the performance of the global model. Although the global reanalysis uses the upper-air observations (and the surface synoptic data over the ocean), the diurnal cycle of temperature and humidity and the surface fluxes over land are all calculated from the model land-surface parameterizations. By studying both the seasonal cycle, the day and night differences, and the diurnal cycle on days with and without rainfall, we will look not for exact detailed agreement between model and observations, but for indications of systematic bias; situations where the model parameterizations

do not represent the data in a realistic way. This both gives the user a sense of the quality of the reanalysis, as well as indicates directions for further model improvements in the model land-surface and BL formulations. The comparison is particularly useful since the FIFE data were not used either in the reanalysis or in the development of the model parameterizations. Many of our conclusions are relevant to the summer 1995 operational MRF model, which is the same model version used for the reanalysis, but with the higher T-126 horizontal resolution. An extended technical report is available from the authors (Betts et al. 1995), since it has been necessary for brevity to omit some of the figures here. The appendix summarizes the model land-surface, BL, and convection parameterizations that are relevant to this study.

## 2. Products used for comparison

Both the raw data and most of our averaged time series are available on CD-ROM (Strebel et al. 1994). The details of the production of our average data are in the appendix of Betts et al. (1993). The editing of the raw data involved both the use of simple range filters and extensive manual editing of bad data. There were data from up to 10 surface portable automated meteorological (PAM) stations in each 30-min average. Since the publication of Strebel et al. (1994), this averaged meteorological time series has been extended to the end of 1987 (Betts et al. 1996), and we use here the average time series from June to October 1987. A similar average time series for 1988 and 1989 is nearing completion. We also averaged the surface flux data (labeled FLUX data on figures) from 17 selected surface sites, which took measurements during the four intensive field campaigns (IFCs). For the seasonal trends and for one period in late July (between IFCs), we shall use a two-station average of data from Smith et al. (1992a), who generated a continuous flux time series for the whole summer. This dataset was used in Betts and Ball (1995). The upper-air data we use was from visually tracked radiosondes (Sugita and Brutsaert 1990a,b), which were launched roughly every 90 mins on almost all sunny days. This data is available also on Strebel et al. (1994) both as raw data (resolution a few hectopascals) and interpolated to standard 5-hPa levels. We used the 5-hPa data, whenever we averaged data from different days. The vertical resolution of the sonde data is much finer than the MRF model, so we reduced the sonde data vertical resolution to 20 hPa (by averaging) to give a fairer comparison. We shall show the diurnal rise of the BL for several pairs of days during the season. The MRF sounding data was simply averaged in the model sigma coordinates.

We show a series of different comparisons between the FIFE data (centered near  $39^\circ\text{N}$ ,  $96.5^\circ\text{W}$ ) and a comparison grid point of the NCEP–NCAR reanalysis (T-

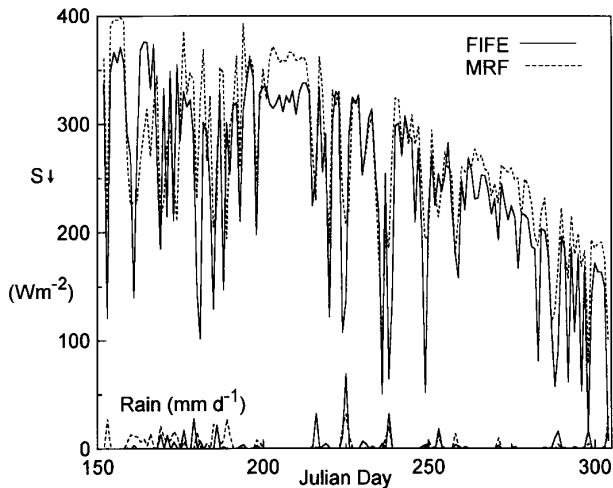


FIG. 1. Comparison of daily averages of incoming solar radiation ( $S\downarrow$  upper curves) from FIFE (solid) and MRF reanalysis (dashed) for 1987. Lower curves are daily precipitation (mm) with data solid and model dashed.

62 grid point centered at  $39.15^{\circ}\text{N}$ ,  $97.5^{\circ}\text{W}$ ). First, we compare the seasonal cycle of the surface energy budget in the data with the 6-h surface flux averages in the reanalysis archive. Then we shall compare the surface daytime diurnal cycle over the season, using the FIFE data and instantaneous 6-h values from the reanalysis archive. After this, short-term (24-h and one 48-h) forecasts from the reanalysis (with the same model at a higher spatial resolution of T-126 using a comparison grid point at  $39.21^{\circ}\text{N}$ ,  $96.56^{\circ}\text{W}$ ) are used to show in more detail how well the model reproduces the observed diurnal cycle for the surface and BL for selected days in June, July, August, and October 1987.

### 3. Seasonal comparison with the FIFE data

This comparison uses the FIFE data and the reanalysis archive of 6-h mean surface fluxes (accumulated from short-term 6-h forecasts) and surface meteorological data every 6 h (which are instantaneous values at each 6-h analysis time).

#### a. Surface flux comparison

We first combine four of the 6-h surface flux averages to give the daily average, and compare this day-averaged data with the FIFE data.

Figure 1 shows incoming solar radiation  $S\downarrow$  ( $\text{W m}^{-2}$ ) from the FIFE PAM data and precipitation ( $\text{mm day}^{-1}$ ) for the five months from June to October (Julian day 152–304). The dotted curves are the model, while the solid curves are the data. The general agreement is fairly good, showing the pattern of rainy days and dry periods. The highest model values for incoming solar radiation exceed these observed during dry periods

(e.g., 202–212 in late July), suggesting the model atmosphere is too transparent. On rainy days, the observed minima are generally also lower, suggesting that cloudiness is underestimated in the model. This excess incoming energy is partly offset in the surface energy budget, because the model albedo at this grid point is 24%, while that for the data is somewhat lower (18%–21%; see Betts et al. 1993). The model shows most of the major precipitation episodes (recall that the data is a much smaller domain than the model grid square), but the distribution shows some differences. The model has much more precipitation in June and early July; less in August and October than was observed (and a little more in September, which was a dry month). This will have some impact on the time sequence of evaporation in the model. The excess precipitation in June and early July appears to be linked to a deficiency in the model surface diurnal cycle caused by feedbacks between several model parameterizations (see section 4a). The total 5-month precipitation in the model is 495 mm, a little more than the 410 mm observed at the FIFE site. The diurnal distribution of precipitation is also different (not shown): 72% of the model precipitation falls in the daytime hours (1200–2400 UTC), whereas 57% is observed to fall at night. The model often rains in the morning before local noon (see section 4a); this is rarely observed.

Figure 2 shows net radiation (RNet) and ground heat flux (plotted as  $-G$ ). The dotted lines are again the reanalysis; while the solid lines are now from the Smith data. The dashed RNet line is an average of the PAM net radiometers. The model ground flux is generally less than the data in June and July. The difference between the solid and dashed RNet curves is an indication of calibration uncertainties in the net radiation data (Smith et al. 1992b), which change sign during the season. Comparing model and data, the net radiation

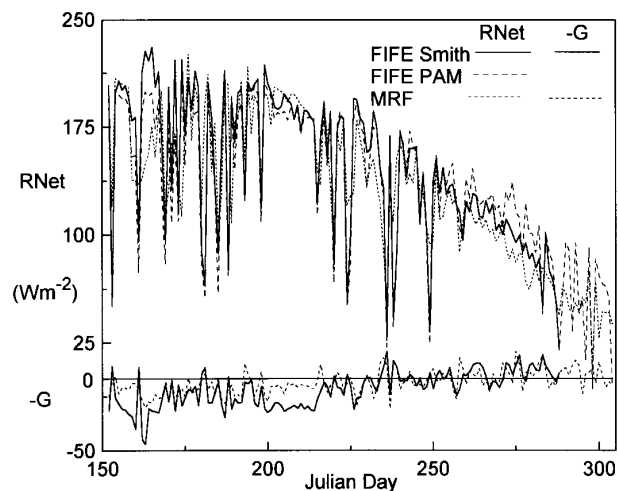


FIG. 2. As in Fig. 1 but for net radiation (RNet) and ground heat flux as ( $-G$ ).

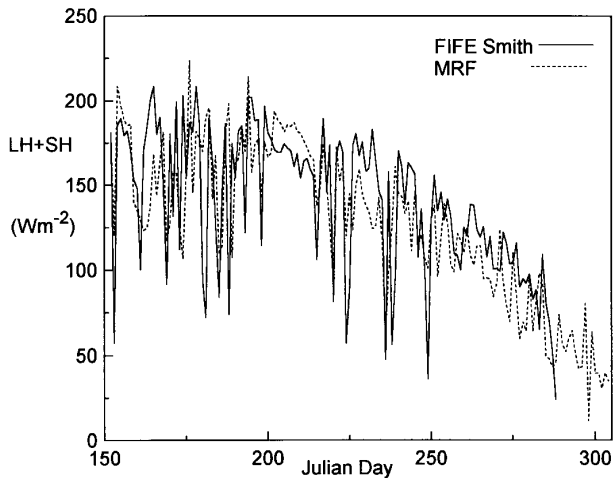


FIG. 3. As in Fig. 1 but for sum of surface sensible (SH) and latent heat (LH) flux.

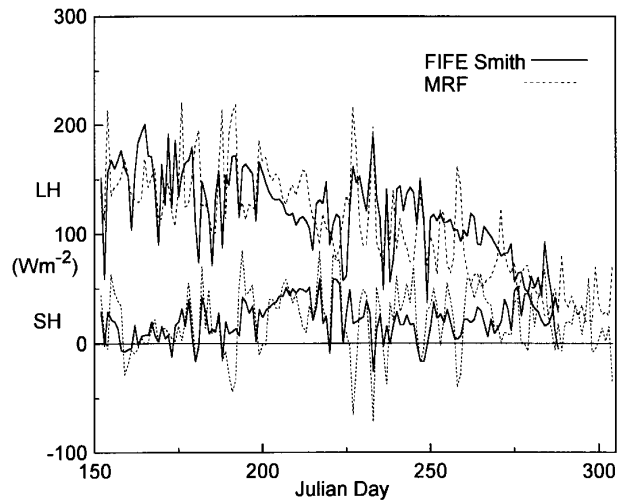


FIG. 4. As in Fig. 1 for SH and LH fluxes.

differences are less than the differences in  $S\downarrow$  in Fig. 1, both because the model albedo is greater, and the model net longwave bias (not shown) is upward relative to the data. In September, the model net radiation is less than observed. Figure 3 compares the sum of sensible and latent heat (SH + LH) from model and data; these satisfy the energy balance  $R_{Net} - G = SH + LH$ . The Smith data ends on 16 October. Averaged over the whole period they agree closely, although there are periods when the model and data differ by  $\pm 15 \text{ W m}^{-2}$ . The total surface energy flux in the reanalysis is generally less than the data in September and October. Figure 4 shows separately SH (lower curves) and LH (upper curves). Although there is some agreement, particularly in long-term means, the model generally swings between larger extremes, with a time frequency of several days. Since SH and LH compensate, we see in the reanalysis matching pairs of high evaporation and large negative sensible heat flux in some 24-h averages. There are also occasions where the model SH flux exceeds any values observed in the summer.

These differences can be understood more easily from separate day and night comparisons, because the behavior of the MRF reanalysis model is significantly different day and night. The 12-h averages (0000–1200 and 1200–2400 UTC), correspond closely for the FIFE area to night and daytime averages (local noon is 1820 UTC). The middle section of Fig. 5 shows the nighttime SH and LH fluxes; below we show the 24-h precipitation and at the top the nighttime wind speed at 0600 UTC (on a reversed scale). The solid SH and LH curves with little variation are the data, and the dotted curves with large extremes are from the reanalysis. There are nights with a mean evaporation of  $150 \text{ W m}^{-2}$  and a corresponding large downward sensible heat flux. For most nights, the reanalysis fluxes are larger in magnitude than the observations. An im-

portant part of the reason for this is that the model does not explicitly switch off evapotranspiration at night. The extreme values appear to be on nights of higher wind. The transfer coefficients in this stable regime may also be too large in high winds. Most of the extremes seen in Fig. 4 for the diurnal averages come from these extremes at night.

Figure 6 compares the daytime LH and SH (with sign reversed) together with the 24-h precipitation. The ranges in model and data are now much more comparable. During the daytime, the larger extremes in the reanalysis follow precipitation episodes. Figure 7 shows the daytime mean surface evaporative fraction (EF) below, and the daily precipitation at the top. The observed EF falls from values close to 1 in early June, when soils are moist, to a minimum around 1 August

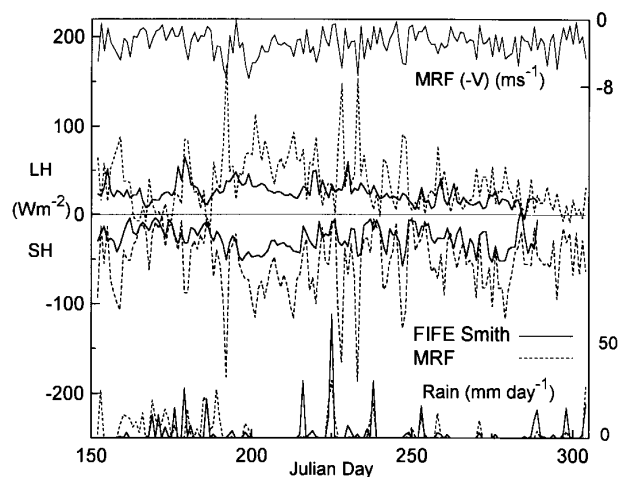


FIG. 5. Comparison of nighttime averages (0000–1200 UTC) of SH and LH fluxes (middle curves). Lower curves show daily precipitation; upper curve is model wind at 0600 UTC (sign reversed).

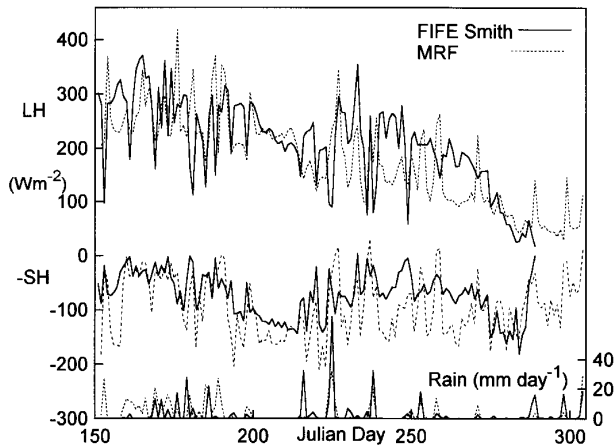


FIG. 6. Daytime averages (1200–2400 UTC) of LH and SH (sign reversed) fluxes. Middle curves are daily total precipitation.

after a period in late July with no rain. The EF then fluctuates in August following rainfall events and falls in the first half of October as the vegetation dies back. Although the reanalysis EF generally follow this seasonal pattern, the rise and fall of EF in the model associated with rainfall events are more extreme than observed, particularly in August. During rain events, the model peaks are higher. After rain the reanalysis EF falls rapidly in a day or two, much lower than the observations. In August and September, the model often has a daytime mean EF  $\approx 0.4$ , that is lower than the value reached in the data in early August at the end of an extended dry period. The low model values around day 222 (10 August) can in part be explained by there being no significant rain in the reanalysis on 4 August (day 216). However, the lower reanalysis evaporative fractions around day 195, day 230, and day 265, which are shortly after significant rain in the reanalysis, suggest that improvements may be possible in the coupling of the vegetative resistances to the soil moisture. At present, the deep soil moisture reservoir is not recharged even by a heavy rain event. The high-frequency fluctuations of EF in summer, shown in Fig. 7, suggest that the present two-layer soil moisture formulation does not represent properly the intermediate timescales of order a week. Betts et al. (1993) noted even greater fluctuations in the surface EF for this time period in an earlier version of the ECMWF model.

In a climatic sense the seasonal cycle of the surface fluxes in the MRF reanalysis (from May to October in Fig. 7) are quite good. We see though some significant differences between model and data, and between the daytime and nighttime behavior of the model. We will explore these differences further in sections 4, 5, and 6 using short-term forecasts from the reanalysis to look at the diurnal cycle. First, however, we will compare the seasonal behavior of the surface diurnal cycle.

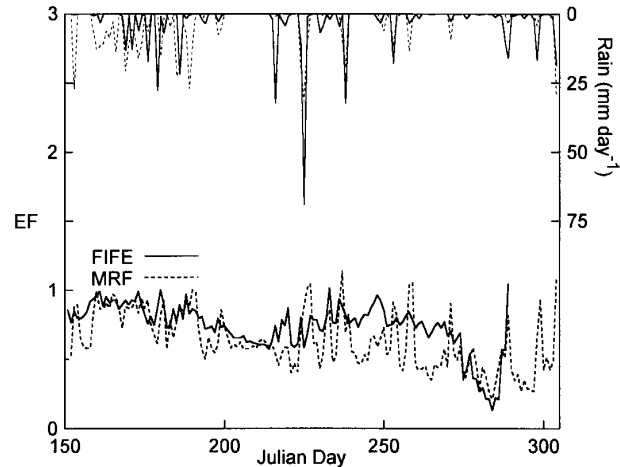


FIG. 7. Comparison of daytime surface evaporative fraction (EF; bottom curves) and daily total precipitation (upper curves).

### b. Diurnal cycle in reanalysis

The reanalysis archive has near-surface atmospheric parameters every 6 h, calculated at the analysis times of 0000, 0600, 1200, and 1800 UTC. Figure 8 shows the comparison of the monthly mean surface diurnal cycle of potential temperature  $\theta$  against mixing ratio  $q$  for the model (dotted) compared with the same average from the FIFE data (solid lines). We show only three values at 1200, 1800, and 2400 UTC, joined by lines. In each case the lowest  $\theta$  value is at 1200 UTC. These represent quite well the daytime diurnal cycle, as they correspond roughly to local solar times of 0600, 1200, and 1800. There is a large change in potential temperature in the morning, when the BL is shallower, followed by much smaller changes in the afternoon when

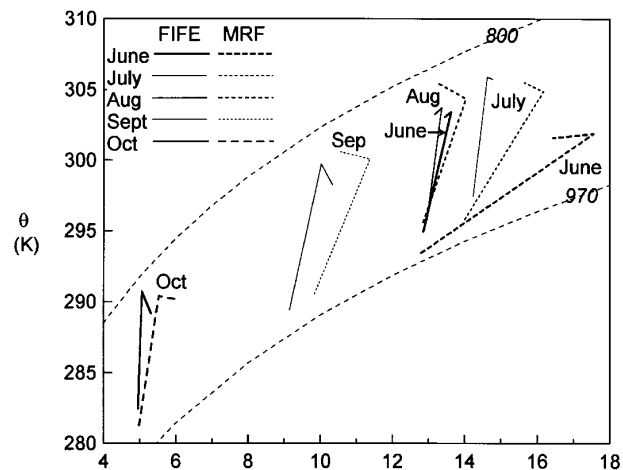


FIG. 8. Comparison of monthly averaged daytime diurnal cycle of potential temperature and mixing ratio at 2 m. Values at 1200, 1800, and 2400 UTC are connected by lines (see text).

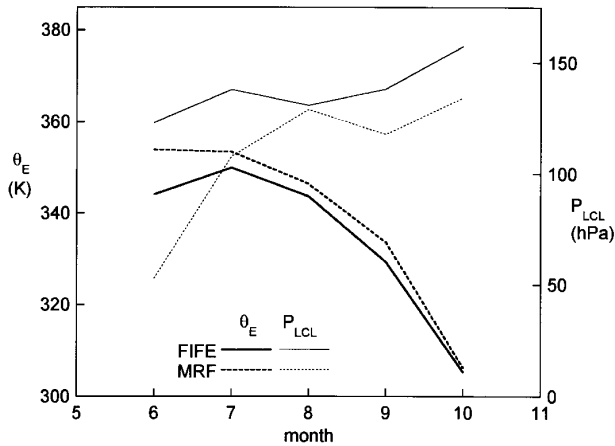


FIG. 9. Comparison of monthly averaged surface  $\theta_E$  (equivalent potential temperature) and  $P_{LCL}$  (pressure height of LCL above surface).

the BL reaches a much deeper quasi-equilibrium for a brief period. The data is shown solid and the reanalysis dashed. The light-dashed lines marked 970 (approximately the surface pressure) and 800 correspond to saturation at these pressures (hPa), so that the daytime rise of saturation level or lifting condensation level (LCL) can be seen. The agreement in July, August, September, and October is good for the monthly mean diurnal cycle. At sunrise, the near-surface air is less than 50 hPa from saturation, while in the afternoon, the  $P_{LCL}$  has risen to 150 hPa.

Typically the model is slightly moister than the data. The reanalysis in June, however, (heavy dashes) has a much moister (and cooler) mean diurnal cycle, than the data in June (heavy solid, indicated with an arrow). The morning rise of  $q$  in the model is  $5 \text{ g kg}^{-1}$ , instead of  $1 \text{ g kg}^{-1}$  in the data, a huge difference. We saw in Fig. 1 that precipitation in June was higher in the reanalysis than observed. The different diurnal behavior appears to be linked to this, and we shall discuss this more thoroughly in section 4a.

Figure 9 shows the monthly mean equivalent potential temperature  $\theta_E$  and  $P_{LCL}$  (the pressure height of the LCL; an estimate of cloud base) at 1800 UTC (near local noon) for the reanalysis (dashed) and data (solid). The data show a peak  $\theta_E$  in July of 350 K, and then a steady fall in succeeding months as the surface and BL become cooler and drier. There is a weak rise of  $P_{LCL}$  during the season. Generally, the reanalysis is about 2 K higher in  $\theta_E$ , and 20 hPa lower in  $P_{LCL}$ . In June, however, this  $\theta_E$  bias exceeds 10 K, and the near-surface air in the model is also much closer to saturation. At noon  $P_{LCL}$  is only 50 hPa above the surface, whereas  $P_{LCL} = 120 \text{ hPa}$  in the data (as can be also seen in Fig. 8). These model differences in June are clearly significant in terms of the feedback between the

surface and convection, and are examined in the next section.

Figure 10 compares two averages of the diurnal cycle of the surface wind. In summer (June, July, and August), the observed wind speed (at 5.4 m) is uniformly stronger than the model (for 10 m). In fall (September and October) the observations have a stronger diurnal cycle than the model.

#### 4. Model behavior in June

Because the reanalysis has excessive daytime rain in June and correspondingly high noon values of  $\theta_E$ , we looked more closely at the possible surface interactions responsible in the model. There are many days in the middle of June (and some in early July), when it rained during the daytime in the reanalysis, and the daytime diurnal cycle was quite unlike any days that were observed. On these days (9–15 and 18–23 June, 4–5 and 8–9 July are examples), the air near the surface remained nearly saturated in the morning after sunrise. On many days, the relative humidity stayed above 90% all day.

##### a. Mid-June morning rainfall anomaly

For the period 11–15 June there was no rain at all at the FIFE site; while at the model grid point there was rain during the daytime period on each day. For the subsequent similar period of 18–23 June, again there is rain at the model grid point during the daytime on each day. On three days (18, 20, and 22 June), it rained at the FIFE site in the early afternoon, while on 19, 21, and 23 June, it did not rain. Figure 11 contrasts the daytime diurnal cycle from 1200 to 2400 UTC for three averages. The squares mark the diurnal cycle for the average of the group of three “dry” FIFE days, with

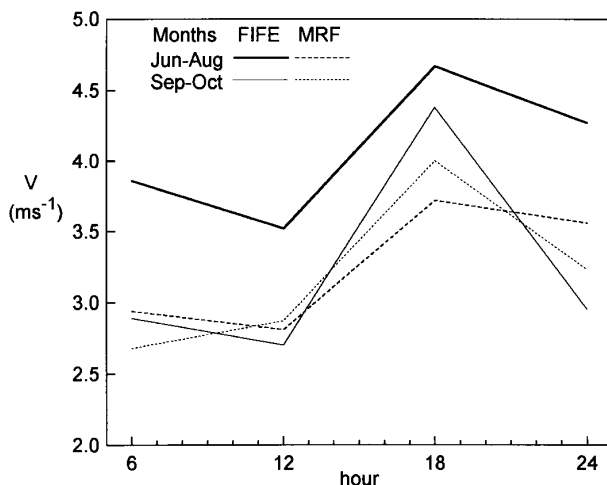


FIG. 10. Comparison of diurnal cycle of surface wind speed for June, July, August average; and September, October average.

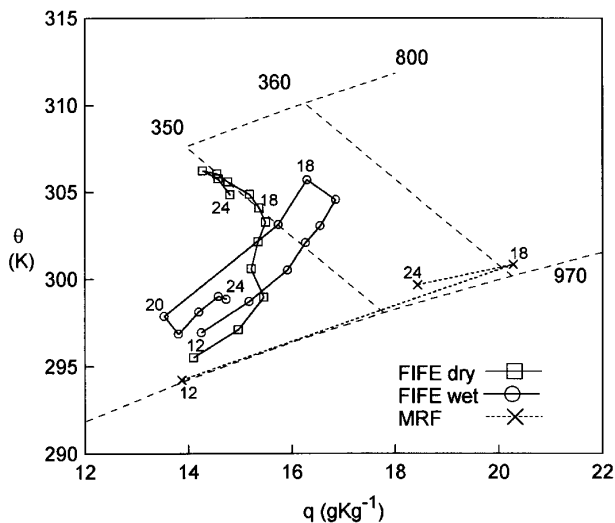


FIG. 11. Daytime diurnal cycle (on  $\theta$ - $q$  plot) for MRF for 6-day average 18–23 June compared with group of 3 dry days (19, 21, and 23 June) and 3 days with afternoon showers (18, 20, and 22 June).

the typical diurnal cycle in which  $\theta_E$  rises to around 350 K and saturation pressure lifts to 820 hPa (the pressure of the LCL) in the afternoon. The data are hourly averages from 1200 to 2400 UTC. The circles are the average of the three days with early afternoon rain. Here we see  $\theta_E$  rise faster in the morning hours reaching 355 K at 1800 UTC (near local noon). Rain follows, and there is a sharp fall of both  $\theta_E$  and LCL with the rain. This is associated with evaporation driven downdrafts bringing low- $\theta_E$  air to the surface (see, e.g., Betts 1976, 1984). In sharp contrast, the 6-day average (dotted) from the reanalysis (for which all days were very similar), shows near-saturation at the surface all day. Equivalent potential temperature  $\theta_E$  rises above 360 K by 1800 UTC. On all days it rains morning and afternoon. For the earlier period 12–15 June, the model behaves similarly, but by 1800 UTC the surface reaches an even higher  $\theta_E \approx 380$  K and a mixing ratio of 24.5 g kg<sup>-1</sup> (not shown). It is clear that the coupling between the surface fluxes, precipitation, and the surface diurnal cycle is quite different in the MRF reanalysis model than is observed. One obvious reason from Fig. 11 is that the model may not adequately represent unsaturated convective downdrafts, which sharply end the rise of  $\theta_E$  once it rains. The model uses a modified Arakawa–Schubert parameterization for convection, discussed briefly in the appendix section (c). However, there is the more fundamental question of why it rains in the model soon after sunrise on these days.

To explore this more closely, we ran a 48-h forecast from 1200 UTC 20 June. We found several possible causes contributing to the unrealistic model behavior. Figure 12 shows the 48-h forecast of model rainfall, model available energy (RNet -  $G$ ), computed potential evaporation  $E_p$ , surface SH and LH fluxes, as well

as the three components of the LH flux from the soil  $E_{soil}$ , evapotranspiration  $E_t$ , and direct evaporation off the wet canopy  $E_c$ . The SH flux is small and the LH flux is close to the potential evaporation. The largest contribution comes from evaporation off the wet canopy, and the second largest is from the wet soil. Evapotranspiration is small because the canopy is wet. Even though the model atmosphere is close to saturated at the surface, evaporation continues at the potential rate from the wet surfaces. Figure 12 shows that one problem contributing to the rainfall is the delayed cloud radiation feedback. The shortwave calculation is only updated every 3 h. The rain starts in the model at forecast hour 3 (1500 UTC) and from 3 to 6 h it rains about 1 mm h<sup>-1</sup>: this keeps the surface wet. The (RNet -  $G$ ) remains very high during this period (reaching 600 W m<sup>-2</sup> at 6 h just before local solar noon), because the incoming shortwave does not see the precipitating clouds until the next radiation update. This drives the large-surface evaporation. At 6 h, the shortwave scheme “sees” the clouds, (RNet -  $G$ ) falls 250 W m<sup>-2</sup>,  $\theta_E$  falls 3 K at the surface, and the rain stops for the next 2 h. Something similar happens on the next day. More frequent updates of the cloud fraction in the radiation scheme would reduce this on and off behavior. The 250 W m<sup>-2</sup> fall in RNet with precipitation in the model is also only half that observed, if we compare the afternoon RNet values for the dry and wet averages in Fig. 11 (not shown). The underlying issue here is the need for compatibility between the parameterizations for convective rainfall, cloudiness, canopy water reservoir and the radiation field in global models with a relatively coarse grid. Convective precipitation and these associated fields are all patchy; that is they have typically smaller scales than the 100–200-km grids we are using here. This model (and many others) does not treat precipitation as patchy (except in an ad hoc way

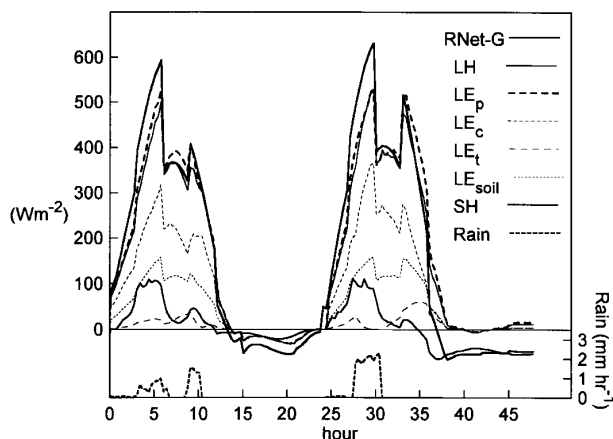


FIG. 12. The 48-h forecast from 1200 UTC 20 June, showing components of the model surface energy fluxes together with model precipitation.

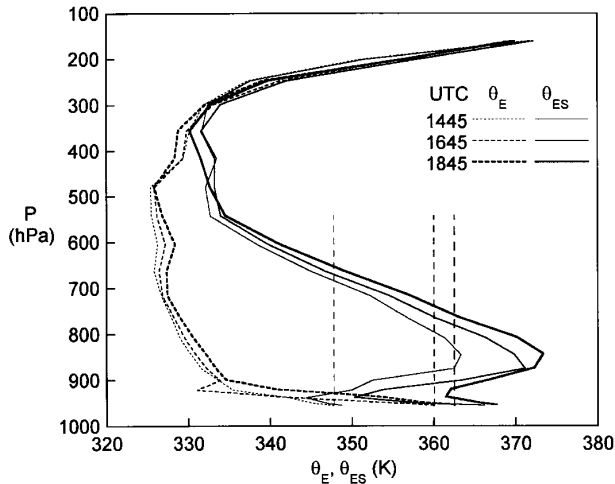


FIG. 13. Model forecast profiles of  $\theta_E$ ,  $\theta_{ES}$  for the morning of 21 June at 1445, 1645, and 1845 UTC (local noon is 1820 UTC).

in the runoff formulation), and, as we have seen, the radiation scheme is not updated for cloud cover on convective timescales.

Figure 13 shows the model profiles of  $\theta_E$  and saturation equivalent potential temperature  $\theta_{ES}$  against pressure for the time period spanning the morning rain on the second forecast day (21 June). These show that the formulation of the convection scheme is also playing some role in permitting rain. The vertical dashed lines are drawn through the surface  $\theta_E$  for the three times. Even though there is an inversion with a  $\theta_{ES}$  maximum near 850 hPa, rain starts at 27 h (1500 UTC 21 June). This is unrealistic. The convection scheme, as formulated, does not see this inversion, which, therefore, plays no role in restricting deep convection. Once rain starts, the inversion itself warms steadily with the convective heating, and the surface  $\theta_E$  continues to rise, driven by the surface evaporation into a shallow layer.

The key reason, however, why the model surface diurnal cycle does not resemble the data is that the surface fluxes in the model are not mixed through a deep layer. Figure 13 shows that the model “mixed” layer (up to the first  $\theta_{ES}$  minimum) is barely 20 hPa deep, whereas on this day in FIFE, the mixed layer grew to 120 hPa in depth by local noon (not shown). With potential evaporation, a nearly saturated surface, and little vertical mixing, the local change at the surface (on a  $\theta$ - $q$  diagram) is indeed a vector nearly parallel to the surface pressure as seen on Fig. 11 (see Betts 1994). With no vertical BL development, all the surface  $\theta_E$  flux goes into a shallow layer and  $\theta_E$  increases, maintaining precipitating convection.

The model lacks several key negative feedbacks. The incoming net radiation responds only every 3 h to clouds. The convection scheme can produce precipitation even in the presence of a BL inversion, and it does not reduce BL  $\theta_E$  through downdrafts. Vertical

mixing in the model is limited by the downgradient BL diffusion scheme. The model formulation of potential evaporation is also suspect. This formulation was originally introduced in the MRF model to reduce evaporation from the bucket model (Pan 1990) in dry atmospheric conditions. In June 1987 in the reanalysis, surface conditions are near saturation. Evaporation in the model stays close to the potential rate (which is of order  $300 \text{ W m}^{-2}$  for a daytime average in mid-June), even when the relative humidity stays near 100% in the morning hours. It is not clear that the evaporation, surface wind speeds (which are low on 20–21 June), and the thermodynamic structure near the surface are all consistent. This needs further investigation. The FIFE data show that as the surface and BL warm and moisten after sunrise, cloud-base always lifts as drier air is mixed down from above (Betts and Ball 1995). In the MRF model (which has little vertical mixing), in these wet surface conditions, the surface stays cool and saturated, and a large latent heat flux modifies only a shallow layer, producing high values of  $\theta_E$ , which trigger precipitation and the feedbacks we have seen.

*b. Late June diurnal cycle*

In late June, there was a break in the pattern of morning rain in the reanalysis. We compare in Fig. 14, the surface energy balance for a 2-day average, 26 and 27 June (which were similar dry days in FIFE), using 24-h forecasts starting at 1200 UTC from the reanalysis, again with the same MRF model at T-126 resolution. In descending order the pairs of curves are RNet, LH, SH, and  $-G$  fluxes with the FIFE FLUX data solid and the MRF reanalysis dotted. The agreement is good considering the fluctuations in cloud cover in both the data and model. The ground flux is less peaked in the model than the data. The fall of SH and rise of LH near fore-

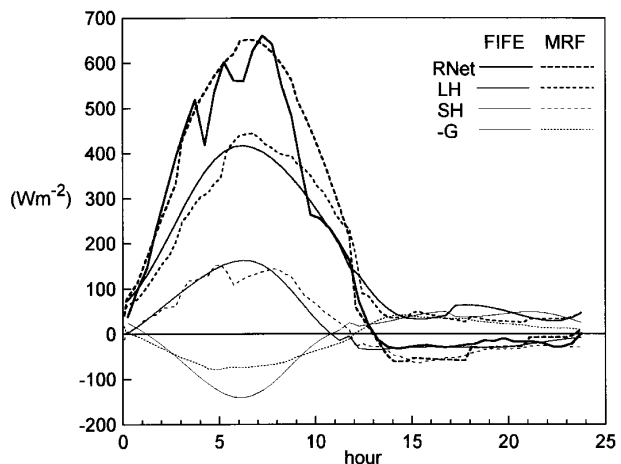


FIG. 14. Comparison of average model 24-h forecasts of surface fluxes from 1200 UTC on 26 and 27 June with FIFE data for same periods.

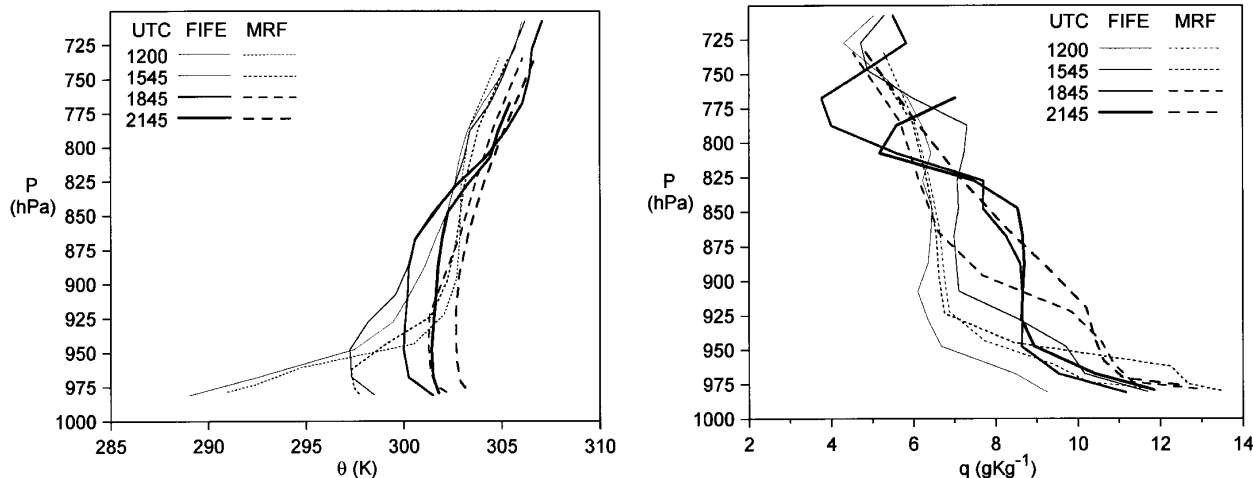


FIG. 15. (a) Comparison of profiles of  $\theta$  against pressure for 26 and 27 June average, showing selected times in the daytime diurnal cycle, starting near sunrise. (b) As in (a) but for profiles of  $q$  against pressure.

cast hour 5 (1700 UTC) in the model is associated with a very brief shower in the model on 27 June. Figures 15a and 15b compare the BL evolution for model (dashed) and data (solid) for the 2-day average. By afternoon the model has produced a nearly well-mixed layer. However, although the surface fluxes are modeled quite closely, we see that the model BL is shallower by about 40 hPa in the afternoon. The model has a noticeably less well mixed structure in mixing ratio  $q$  than the data, and a slightly weaker surface superadiabatic layer. Figure 16 compares the surface daytime diurnal cycle of  $\theta$  and  $q$ . Lines corresponding to saturation at the surface pressure (980 hPa) and 800 hPa, and  $\theta_E = 330, 340$  K are shown dashed. The model forecasts the diurnal rise of  $\theta$  well, but the model is

considerably moister than the data at the surface throughout the day. The data are plotted hourly from 1215 to 2315 UTC for both the FIFE 2-day mean and the MRF mean. The small numbers denote the hours. The poor vertical mixing of  $q$  shown in Fig. 15b, the extra rain in June, and generally higher LH fluxes at night are probably all linked to these higher mixing ratios near the surface. The model surface starts near saturation at the surface pressure of 980 hPa at 1215 UTC, and cloud base rises more slowly than in the data, presumably because of the reduced vertical mixing in the model. Similarly, the model  $\theta_E$  remains a few kelvins higher than the data throughout most of the day.

### c. Summary of model behavior in June

In June, several features of the model appear to interact to produce excessive daytime rain in the reanalysis. High (“potential”) evaporation into a shallow layer with too little vertical mixing produce a near saturated condition with high  $\theta_E$ . This triggers the precipitation in the convection scheme (which does not see the BL inversion). The clouds are not seen by the radiation scheme for several hours, so the surface net radiation is not reduced quickly by clouds. The convection scheme, unlike precipitating convection in the atmosphere, does not reduce BL  $\theta_E$  through downdrafts, so the model lacks negative feedbacks to reduce the rise of  $\theta_E$  near the surface. However, by late June, when the atmosphere is drier, this anomalous model rain disappears. In late June the model behavior is then quite realistic, although the BL growth is somewhat less than observed. The excess daytime rain reappears again in early July, and then finally disappears for the summer, probably because the soil dries out during an extended dry period. Many of the details of these model feedbacks are still being investigated further. Hong and

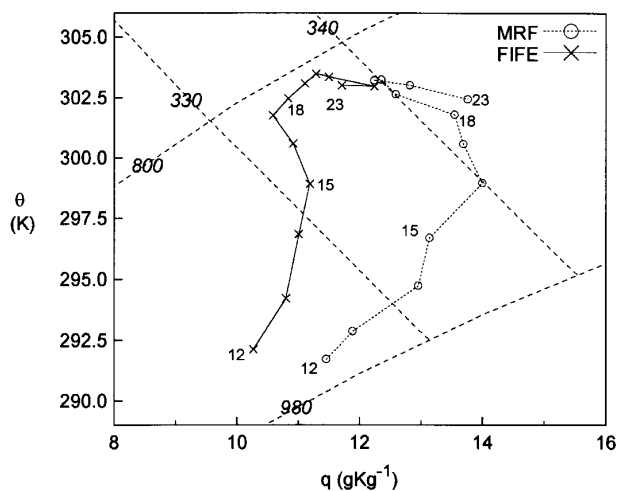


FIG. 16. Daytime diurnal cycle of  $\theta$  and  $q$  for FIFE data (solid) and MRF (dashed) for 26–27 June average; data is hourly starting at 1215 UTC.

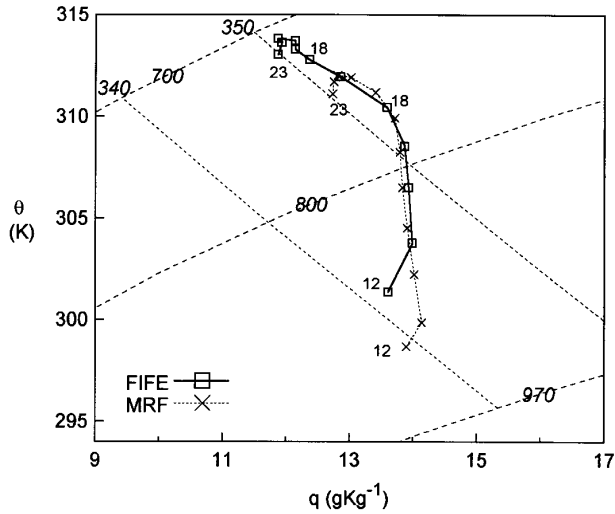


FIG. 17. As in Fig. 16 but for averages of 30 and 31 July.

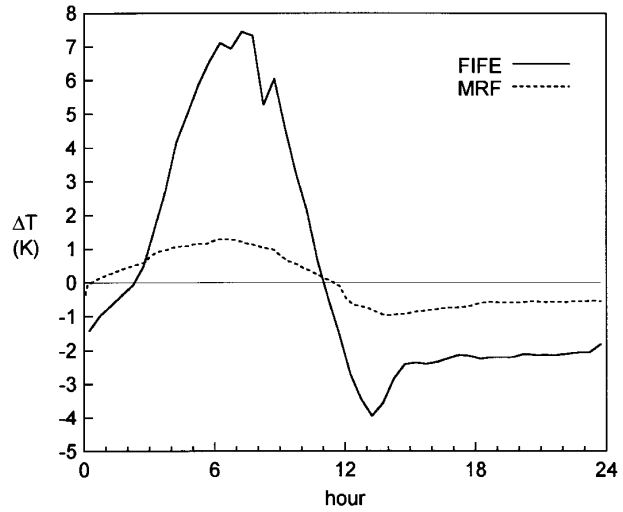


FIG. 18. Comparison of  $\Delta T = T_{\text{surf}} - T$  for model and data for 30–31 July average.

Pan (1996, manuscript submitted to *Mon. Wea. Rev.*) show that introducing a nonlocal BL vertical diffusion scheme and changes to the convection scheme improved the precipitation forecasts in parallel runs during August 1995.

### 5. Midsummer diurnal cycle

After 9 July (Julian day 190) the excess daytime model rainfall, discussed in the previous section, appears to disappear at the FIFE grid point. As observed, the rest of July had little precipitation, soil moisture falls in the model, and the model surface EF falls (Fig. 7). We now present some comparisons from this period.

#### a. Late July dry period

The two days 30 and 31 July were toward the end of an extended dry period of 2 weeks without rain. Observed surface EFs reached their lowest values of the summer (Kim and Verma 1990), and observed air temperature  $T$  and surface temperature  $T_{\text{surf}}$  were at their highest. Again we ran 24-h forecasts from the 1200 UTC reanalysis for each day, and averaged the two to show a mean diurnal cycle. Figure 17 compares the daytime diurnal cycle for model and data. The shape of the diurnal cycle is very similar, although an offset is visible. The model is cooler and for most of the daytime moister than the data. Both model and data reach  $\theta_E \approx 352$  K, but the data has a higher  $P_{\text{LCL}}$  throughout the day by 30–40 hPa. Figure 18 shows the difference  $\Delta T = T_{\text{surf}} - T$ . For the data,  $T_{\text{surf}}$  is a radiometric temperature. In the dry conditions of late July,  $\Delta T$  actually exceeds 7 K at solar noon. In the model, however, this difference barely exceeds 1 K. At night the observed  $\Delta T$  is again larger in magnitude.

The model surface temperature appears to be too tightly coupled to  $T$  at 2 m. This appears to be a general characteristic of the model. Improvements may be possible in the model surface-layer parameterization. The model has the same roughness length for heat ( $Z_{0h}$ ) and momentum ( $Z_{0m}$ ). One study using the FIFE aircraft data (Betts and Beljaars 1993) gave  $Z_{0m}/Z_{0h}$  of order 20. Other studies have suggested that this ratio can be even higher (e.g., Beljaars and Holtslag 1991). Increasing  $Z_{0m}/Z_{0h}$  increases the skin-air temperature difference. The model generates a deep afternoon BL to about 820 hPa (not shown). There is no sounding data for these two days for comparison.

Figure 19 shows the comparison between the model and the Smith flux data (the 17-station average is not available in late July). The RNet values are quite close.

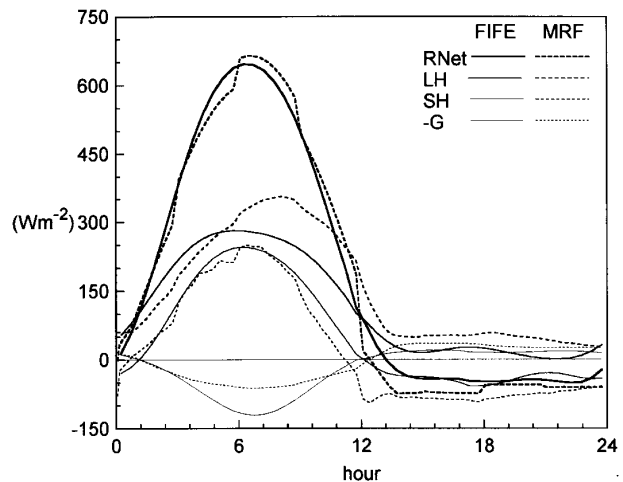


FIG. 19. As in Fig. 14 but for 30 and 31 July average.

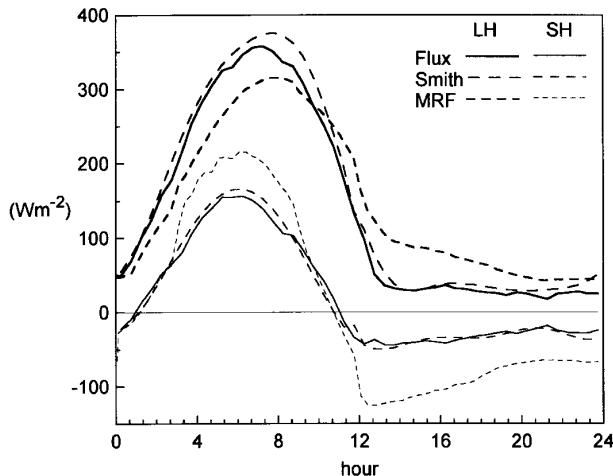


FIG. 20. Comparison of SH and LH fluxes for 9-day August average of 24-h MRF forecasts and FIFE data.

In the afternoon, the model EF of about 0.6 is higher than the observations ( $\approx 0.52$ ). Although these observations are based on only two Bowen ratio stations from Smith et al. (1992a), Kim and Verma (1990) show a still lower afternoon EF of 0.43 at another FIFE site on 30 July. At night, the same pattern is seen (as in Fig. 5) of higher LH and downward SH fluxes in the model. The higher model EF in the daytime in late July and greater model evaporation at night are probably responsible for the cool moist shift of the diurnal curve of the model from the data, seen in Fig. 17. It appears that the model evaporation is higher than the observations toward the end of this dry period. The model 2-m-deep storage reservoir for soil moisture appears to be more than adequate to maintain the surface evaporation for three weeks without rain. However, by 9–10 August, the model EF has fallen further (Julian day 221–222 in Fig. 7), while the observed EF of 0.56 is similar to that in late July. Rain fell on 4 and 8 August, but there was almost none in the reanalysis for these dates (see Fig. 1), so that the soil moisture continued to fall steadily in the model between 30 July and 10 August (days 211–222 in Fig. 23 later). Consequently, the model EF continued to fall from 1 to 10 August.

The surface energy budget and diurnal cycle in the reanalysis appears to be much better in midsummer than in the June period. The model describes well the dry-down following no precipitation in late July. Perhaps surprisingly it maintains a higher surface evaporation than observed. This may be a consequence of the extra rain earlier, stored as soil moisture in the deep 2-m reservoir.

#### b. 9-day August average

We then averaged the diurnal cycle of nine selected days in August from the FIFE 1987 data and the MRF

reanalysis to look at the “representative” midsummer behavior of the model. There is extensive field data for these days. We ran 24-h forecasts starting from 1200 UTC on 6 (Julian day 218), 7, 9, 10, 15, 16, 17, 20, and 21 August. These days had little daytime rain in FIFE, and no daytime rain in the reanalysis. The diurnal curves of RNET (not shown) agree quite closely. For brevity we show only the comparison of mean SH and LH fluxes at the surface. The 17-station flux average are the solid pair of data curves; the two station Smith average (which are slightly higher) are shown long-dashed: they agree well. We consider the 17-station average to be the most representative, and will present it whenever it is available. The model (short dashes) has a higher daytime SH flux and lower LH flux, giving a lower daytime EF near solar noon. However, the pattern reverses by sunset and at night. The model evaporation stays high, and the energy is supplied by a larger downward sensible heat flux in the model than the data. This is the same as the nighttime behavior we saw in the seasonal data in Fig. 5. In fact this group of 9 days includes several of the extreme peaks on Fig. 5, such as day 228. These comparatively large model surface fluxes at night are associated with transfer coefficients that are high for this stable regime, as well as nonzero evapotranspiration at night in the model. We will look at specific cases in the next section.

#### c. August before and after heavy rain

While the 9-day August mean suggests that model averages in midsummer may be quite good, the individual days show that the model tends to greater extremes as suggested by Fig. 7. There was a major rain event on 12–13 August (Julian days 224–225). Figure 21 shows soil moisture (SM) at 1800 UTC for the two model layers for the individual days for which we made

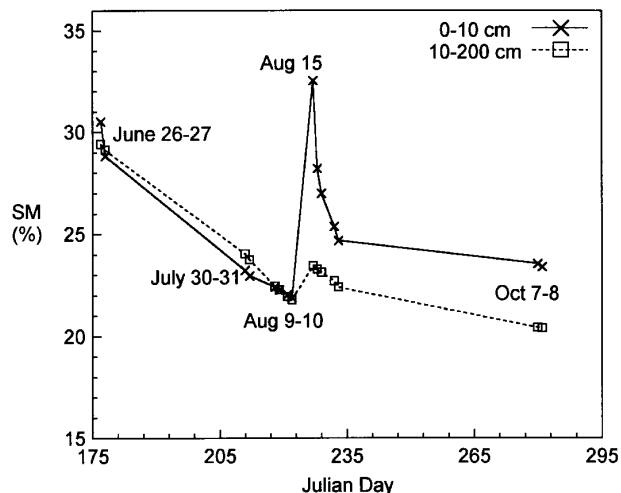


FIG. 21. Soil moisture at local noon for selected days for the two model layers in reanalysis (in percent by volume).

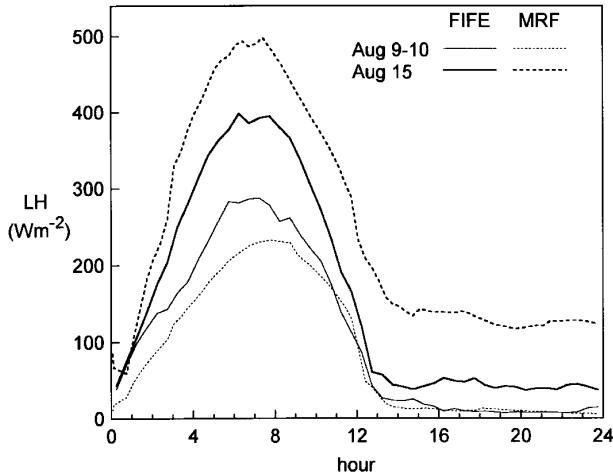


FIG. 22. Comparison of model 24-h forecasts of LH flux with FIFE data for 9–10 August average and 15 August.

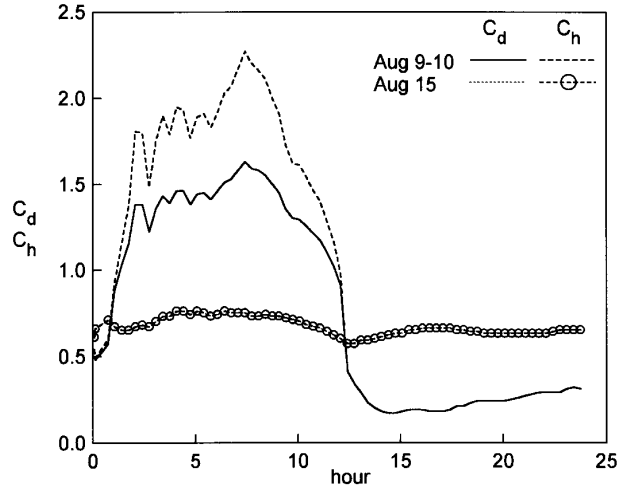


FIG. 23. Model surface transfer coefficients for momentum ( $C_d$ ) and heat and moisture ( $C_h$ ) for 9–10 August average and 15 August.

24-h forecasts. Soil moisture is low in the model on 9 and 10 August before this rain, and then declines from a peak in the period 15–21 August after the heavy rain event. Note that although much of the heavy rain that fell reaches the second soil layer, the deep soil reservoir is not replenished. We compared an average of the forecasts from 1200 UTC on 9 and 10 August (which were similar days before the heavy rain) with 15 August afterward.

Figure 22 shows the LH flux for the model and the FLUX data for these before and after rain cases. The net radiation curves are similar for model and data (not shown). Following the rain, the observed daytime peak LH flux does rise significantly from 280 to 400  $W m^{-2}$  (solid lines), and the evaporative fraction (EF) increases from around 0.55 to 0.77 (not shown). However, the rise in the model (dotted lines) is much more extreme from 230 to 500  $W m^{-2}$ , while the model EF increases from 0.4 to unity. Correspondingly, with the dry to wet transition, the model noon peak in SH flux drops from 340 to 0  $W m^{-2}$ , while in the data there is a much smaller fall from 240 to 120  $W m^{-2}$  (not shown). The difference at night shows (to a greater extent) the same behavior seen in the August mean in Fig. 20. The observed LH flux is larger on 15 August than 9–10 August, but model LH flux remains high at night around 130  $W m^{-2}$ . There is correspondingly a very large downward sensible heat flux of about 150  $W m^{-2}$  (not shown). These high nighttime fluxes correspond to the spike seen in Fig. 5 for day 228. Figure 23 shows the model surface transfer coefficients for heat and moisture ( $C_h$ ) and momentum ( $C_d$ ). On 9 and 10 August, there is a large diurnal range, but on 15 August, the diurnal range is nonexistent (the surface daytime superadiabatic layer is absent: see later) and the nighttime transfer coefficient is high. The model winds on 15 August are strong at 10 m (5–6  $m s^{-1}$ ),

but still not quite as strong as the winds observed at 5.4 m (6–8  $m s^{-1}$ ). This confirms (as does Fig. 10 previously) that the too high surface fluxes are not due to errors in the surface wind. As we suggested in section 3a in the discussion following Fig. 5, it appears that the model surface transfer coefficients are too large in higher winds; in particular this drives too large fluxes at night. The night of 15–16 August is a good illustration of this. However, a major part of this error is that the model does not explicitly switch off evapotranspiration at night. For this night with high winds about half the evaporation is evapotranspiration. On this day, there is too much daytime evaporation as well with a stable surface layer and moderately strong winds. Both model and data show a fall of the surface–air temperature difference  $\Delta T$  after the rain, but the model diurnal

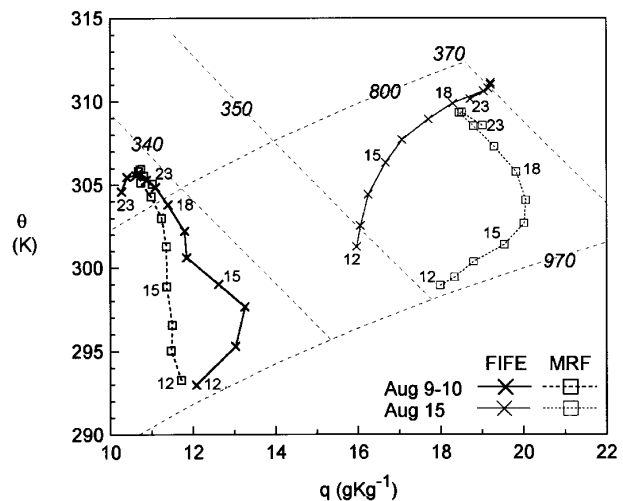


FIG. 24. As in Fig. 16 but for 9–10 August average and 15 August.

range is much smaller both in the daytime and at night (not shown), as seen earlier in Fig. 18 for late July.

Fig. 24 compares the daytime diurnal cycle of  $\theta$  and  $q$  for the two cases. For 9–10 August, the model is a little drier, presumably because the model surface EF is lower, but both model and data reach a similar afternoon state. It appears that reduced BL entrainment of warm, dry air and the lower surface EF in the model appear to compensate. For 15 August, the surface diurnal curves of model and data are very different. The model is cooler by about 2°C throughout the day (and the following night: not shown). Although the diurnal patterns are quite different, remarkably the daytime rise of temperature in the model is 10°C, similar to that observed. How can this be, given near-zero surface SH flux? Horizontal advection may be partly responsible, but the major contribution is a downward eddy transfer of heat of order 80 W m<sup>-2</sup> at 900 hPa. Similarly, there is an upward eddy transport of moisture of order 400 W m<sup>-2</sup> near the surface.

Figures 25a and 25b compare the BL potential temperature  $\theta$  against pressure for these two cases. The observations in Fig. 25a (solid lines) show that 9–10 August had a deep mixed layer with a top near 800 hPa. The data has again been averaged in 20 hPa layers to give a resolution comparable to the model. We have selected four sounding pairs from the eight that were launched on each day. The model reproduces the time evolution rather well for  $\theta$ , but the model mixed layer is noticeably shallower by 30–40 hPa in the afternoon, as in the 26–27 June comparison shown earlier (Fig. 15). The  $q$  profiles (not shown) shows a similar shallower BL in the model. Again the reason is the lack of BL-top entrainment in the model. As shown in Fig. 25b, 15 August is a day on which there was a much shallower BL. The data shows a nearly well mixed BL with a top around 900 hPa (fluctuating about  $\pm 15$  hPa during the day: there are four other soundings not

shown). By midmorning, a weak surface superadiabatic layer is generally present (the sonde surface data shown is cooler than the other surface meteorological data). In contrast the model has a stable BL structure all day, consistent with the near-zero surface SH flux. The model BL stays cooler than the observations all day. There are striking differences between model and data in the  $q$  profiles (not shown). The model  $q$  changes little with time and all profiles show a uniform decrease of  $q$  with height, while the observations show a weak “mixed layer” from 900 to 960 hPa. We can again ask how the model  $\theta$  warms with time, while  $q$  remains nearly constant despite a zero surface SH flux and large LH flux. The eddy transport scheme is transporting heat downward and moisture upward as mentioned above. The BL wind speeds are quite high on 15 August. There is a morning low-level jet approaching 20 m s<sup>-1</sup> in the data and 16 m s<sup>-1</sup> in the model (not shown). Shear-driven turbulence must play a significant role on this day, but the stable transports in the model appear to be rather high in the BL as well as at the surface. They must be partly responsible for the near zero daytime SH flux in the model. Note the compensation of different processes in the model. On 9–10 August, less BL-top entrainment of warm dry air, but a smaller surface EF, appear to largely compensate, so that the daytime rise of  $\theta$  and small fall of  $q$  are similar. Almost the reverse happens on 15 August. The model surface EF is too high, but this appears offset by the downward transports of warm dry air. In both cases we see differences in BL structure.

## 6. October comparison

Figure 26 shows the daytime diurnal cycle for averages of 7 and 8 October, both sunny days after the first hard frost on 1 October. We show points at 1245 UTC (the morning temperature minimum) and then

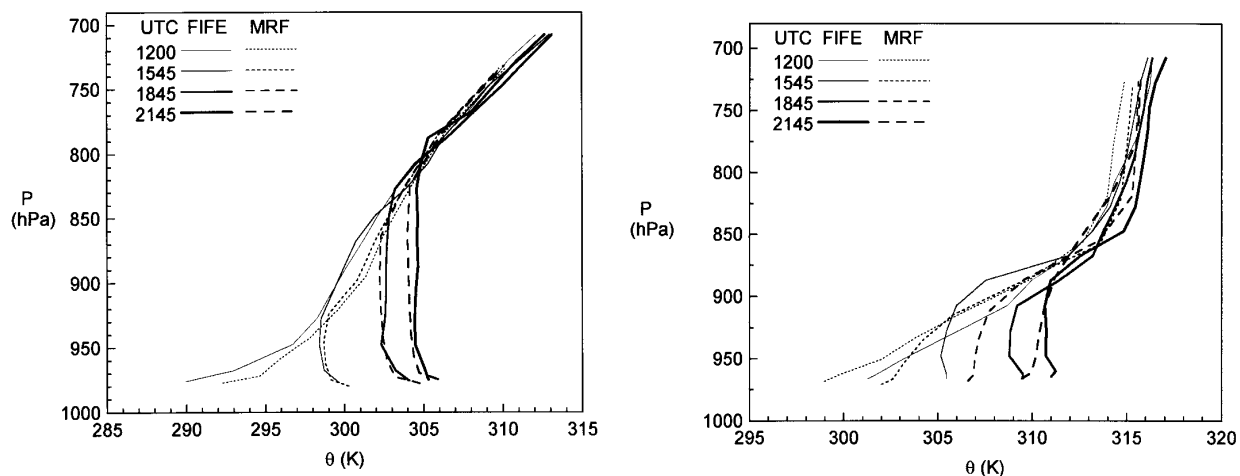


FIG. 25. (a) As in Fig. 15a but for  $\theta$  profile for 9–10 August average. (b) As in (a) but for 15 August.

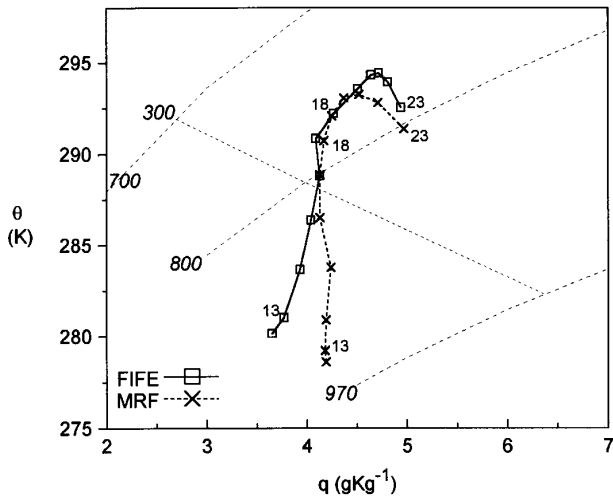


FIG. 26. As in Fig. 16 but for 7–8 October average.

hourly values from 1315 to 2315 UTC. As in late July, the model is systematically a little cooler than the data, but the low mixing ratio in October is modeled closely. Figure 27 shows the surface fluxes, the sequence from top to bottom is now RNet, SH, LH,  $-G$  with the model dashed and the FLUX data solid. RNet is significantly higher in the model. Some of this is the low model  $T_{surf}$ , which reduces outgoing LW, but there is a significant difference of  $60 \text{ W m}^{-2}$  in the net incoming solar radiation at local noon. As in Fig. 1, this suggests that the model atmosphere is too transparent or has too little cloudiness. Betts et al. (1993) saw a very similar difference between the ECMWF model and these observations. The albedo of the FIFE grassland has increased by 2%–3% in the fall after the vegetation has largely died; this increases the reflected solar radiation by at least  $20 \text{ W m}^{-2}$ . However, the model has a fixed albedo of 24%, which is higher than the observed range (see section 3a). In comparison with the observations, the model in October has almost double the daytime LH flux, a larger daytime ground heat flux and a slightly lower SH flux. The observed EF falls steeply in October after the vegetation has largely died and the temperature falls. The model captures only some of this response (Fig. 7), since it has a fixed minimum vegetative resistance at each gridpoint. The model BL deepens to about 860 hPa during the day, not quite as deep as observed (not shown). The BL mixing ratio increases in the model during the day as observed (not shown). Overall the model handles the seasonal transition to reduced evaporation in the fall reasonably well. The observed transition following the first hard frost may be faster than the transition seen in the model, but this can be regarded as a consequence of the fixed minimum vegetative resistance at each gridpoint in the model.

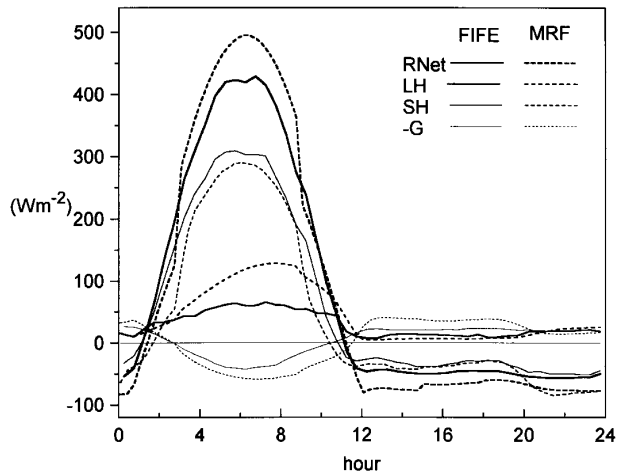


FIG. 27. As in Fig. 14 but for 7–8 October average.

### 7. Discussion and conclusions

The surface fluxes and BL thermodynamic variables feed back in summer through deep convection on the tropospheric temperature, so their accurate simulation is important in a global model (Betts et al. 1996). The long time series dataset from the FIFE experiment has again proved of great use in assessing the quality of a global forecast model, through comparison with the model simulation for a nearby grid point. Since the model used in the reanalysis was also the summer 1995 operational global forecast model at NCEP, our conclusions are relevant to both the reanalysis and the representation of the land surface in MRF forecasts for that summer.

In a climatic sense the seasonal cycle of the day-averaged surface fluxes in the MRF reanalysis are quite good. The comparison of the diurnal cycle of the MRF

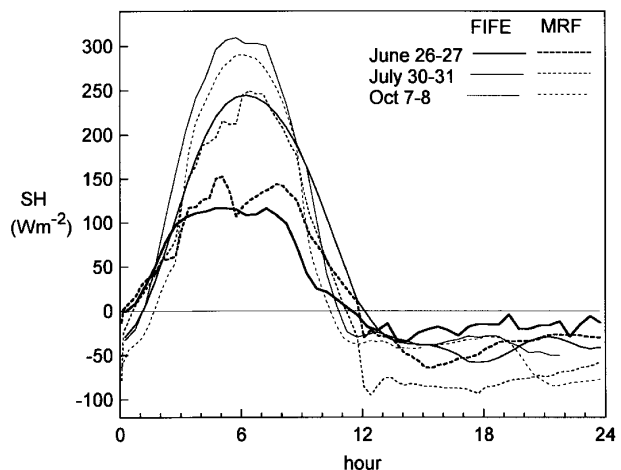


FIG. 28. Comparison of SH flux for model 24-h forecasts and FIFE data for three pairs of days through seasons.

reanalysis over the seasonal cycle with the 1987 FIFE data in Kansas is also encouraging. The model generally reproduces the diurnal cycle of the surface and BL  $\theta$ , and  $q$  to about  $\pm 2^\circ\text{C}$  and  $\pm 2 \text{ g kg}^{-1}$ . Such close agreement reflects improvements in the model land surface parameterizations in recent years. Figures 28 and 29 illustrate this with a snapshot of the season based on three pairs of days in June, July, and October. The seasonal rise of SH flux in the model (dotted in Fig. 28) as the model soil dries and the air temperature falls, follows the data, even though the model does not have an explicit seasonal vegetation cycle. The diurnal rise of the model 2-m air temperature shown in Fig. 29 is within 2 K of the seasonal cycle seen in the data, although the model has a tendency to be cool.

We saw in previous sections some significant differences between model and data, which suggest areas where model improvements are possible. During the daytime, the fluctuations in surface EF in the model following precipitation events are larger in the model than in the data. We also saw big differences between the daytime and nighttime behavior of the model. The surface fluxes at night (evaporation and downward SH flux) are generally too large; they can exceed  $150 \text{ W m}^{-2}$  when wind speeds are strong. Short-term forecasts from the reanalysis confirm these discrepancies. The model (downward) sensible and (upward) latent heat fluxes at the surface are generally too large at night (often by a factor of 2 or more), because the transfer coefficients in this stable regime are also correspondingly large, and the model does not explicitly switch off evapotranspiration at night, which can be large if the wind speed is high. The full impact of these day-night differences in the model is not clear from these 24-h forecasts. They may be more significant in longer term forecasts, where the integrated budget over the whole diurnal cycle is important. We also suggest caution in using the diurnally averaged surface energy budget of the reanalysis for climate studies, where the 24-h integral is important.

One key to an acceptable land-surface scheme is accuracy in the prediction of surface evapotranspiration. In general the MRF model does fairly well in modeling the seasonal fall of evapotranspiration from late June through August to October. The 2-m-deep soil moisture reservoir used in the reanalysis probably has more than enough seasonal storage capacity. However, it is difficult for even heavy rainfall to recharge it. It is never replenished once it has dried out in July. Perhaps more than two soil layers are needed to represent the intermediate timescale (of order a week) in the soil moisture reservoir. The period in August, which we have presented in more detail, does show that natural grassland has greater stability than the model simulation. About 80 mm of rain fell between 10 and 15 August, and the observed surface EF rose from 0.55 to 0.77 near local noon. The corresponding model EF, however, rose much more from 0.4 to near 1, although there was less

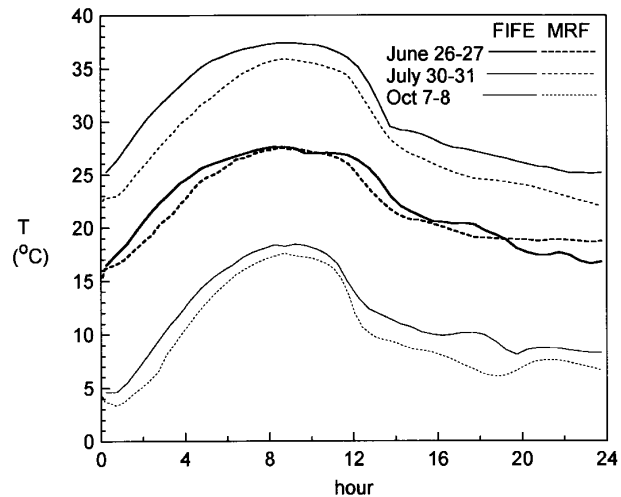


FIG. 29. As in Fig. 28 but for 2-m air temperature comparison.

rainfall in the model. Throughout this 6 to 21 August time period, the observed noon EFs are clustered in a narrower range than those of the model. On 15 August, a windy day with high soil moisture, the surface fluxes in the model remained high both day and night despite a stable BL. The model surface transfer coefficients were high and had no diurnal cycle.

Boundary layer depth is generally underpredicted in the MRF model, because the down-gradient diffusion scheme (Louis 1979) does not properly represent entrainment at BL-top. Analyses of the FIFE data have suggested that BL entrainment plays an important role (Betts 1992; Betts and Ball 1994). However, the model sometimes compensates for this by a stable diffusion process. On one day (15 August) when winds were strong, the model diffusion was sufficient to transport heat downward and moisture upward, even in the absence of a surface sensible heat flux. A new BL scheme is being tested (Hong and Pan 1996, manuscript submitted to *Mon. Wea. Rev.*).

The incoming solar radiation appears to be overestimated in the model, but this is partly offset at the FIFE site by a higher assumed albedo. The reduction of incoming solar radiation by cloud cover is generally underestimated. The update of clouds in the radiation scheme only every 3 h produces significant errors in the surface energy budget, when it first starts to rain. In June and early July there is too much daytime rain in the model. This appears to involve the interaction of several components of the surface, BL, and convection schemes, and is being investigated further. Too little vertical mixing means the surface  $\theta_E$  rises too quickly after sunrise in a shallow nearly saturated BL. The convection scheme, which does not see the BL inversion, often produces precipitation that wets the surface. Evaporation stays high as the incoming solar radiation is not reduced by the cloud fields until the next radia-

tion scheme update. The surface stays wet and nearly saturated at high  $\theta_E$  and light rain of order  $1 \text{ mm h}^{-1}$  persists.

The difference between skin temperature and air temperature is always underestimated in the model in comparison with the data, often by several degrees. In the driest part of the summer the measured radiometric surface temperatures were 8 K higher than the model surface temperature. The reverse is true at night, when the observed radiometric surface temperatures generally fall below the model surface temperature. The implication is that the near-surface heat transfer coefficients for heat are in some sense too high in the model for both stable and unstable regimes. At present the model uses the same roughness length for heat and momentum.

The overall seasonal cycle of the land surface interaction in the reanalysis compares quite well with the FIFE data near Manhattan, Kansas. Not surprisingly, however, we have found several areas where improvements in the model parameterizations are desirable, and may well lead to improved medium-range forecasts. Indeed Hong and Pan (1996, manuscript submitted to *Mon. Wea. Rev.*) have already shown consistent improvements in precipitation forecast skill over the continental United States from introducing a nonlocal BL vertical diffusion scheme, more frequent updates to the radiation field, and improvements in the convective parameterization. The changes they discuss were implemented in the operational MRF model in October 1995.

APPENDIX

**Summary of Key Physical Parameterizations in Reanalysis Model**

The version of the MRF model used in the reanalysis at T-62 spectral resolution was the operational MRF model (at T-126 resolution) from 10 January 1995 to 25 October 1995; when the revisions discussed in Hong and Pan (1996, manuscript submitted to *Mon. Wea. Rev.*) were implemented.

*a. Land-surface model*

This version of the MRF model utilizes the two-layer soil model of Mahrt and Pan (1984) and Pan and Mahrt (1987) with minor modification based on Pan (1990). The soil model includes soil thermodynamics and soil hydrology, both modeled as diffusion processes. The primary feature of the soil model is the use of diffusivity coefficients that are strongly modified by the soil water content. The thickness of the two soil layers in the reanalysis model was 10 and 190 cm. We present the equations for the evaporation model, since this is a key process in the surface energy balance. Evaporation is modeled as three components: direct evaporation from the bare soil surface, transpiration through the leaf

stomata, and re-evaporation of precipitation intercepted by the leaf canopy.

1) DIRECT EVAPORATION

The direct evaporation from the bare soil surface is modeled after Mahrt and Pan (1984). It uses an estimate of the soil water flux at the surface as the evaporative flux (bounded by the potential evaporation [see Eq. (A5)] when the soil is wet):

$$E_{\text{soil}} = (1 - \sigma_f) \left[ -D(\Theta)_0 \left( \frac{\partial \Theta}{\partial z} \right)_0 - K(\Theta)_0 \right], \quad (\text{A1})$$

where  $\Theta$  is the volumetric water content,  $D(\Theta)$  is the hydraulic diffusivity,  $K(\Theta)$  is the soil hydraulic conductivity, and  $\sigma_f$  is the fraction of the grid area covered by vegetation, which is fixed at 0.7 over the globe. The subscript 0 denotes that the quantity is estimated for the first half layer between the middle of the first (10-cm) soil layer and the surface (where a fixed value of  $\Theta$  is specified).

2) CANOPY REEVAPORATION

When rain falls to the ground, the leaves first intercept the rain up to a canopy capacity of  $S$  ( $=0.002 \text{ m}$ ), and the excess drips to the ground. The canopy water then reevaporates at a fraction of the potential rate [ $E_p$ : see Eq. (A5)] as

$$E_c = \sigma_f \left( \frac{C^*}{S} \right)^n E_p, \quad (\text{A2})$$

where  $C^*$  is the amount of canopy water and the factor  $n$  is set to 0.5. The canopy water  $C^*$  is bounded between zero and  $S$ . The interception model is similar to that of Rutter et al. (1971), as described in Pan and Mahrt (1987).

3) TRANSPIRATION

This is the process whereby vegetation extracts water from the root zone and releases it to the atmosphere from the leaf stomata during photosynthesis. The MRF model uses a potential evapotranspiration [ $E_{\text{tp}}$ : see Eq. (A9)], reduced by a soil wetness function and the fraction of the canopy that is dry:

$$E_t = \sigma_f \left[ 1 - \left( \frac{C^*}{S} \right)^n \right] \overline{\beta}_i E_{\text{tp}}. \quad (\text{A3})$$

The soil wetness reduction factor  $\overline{\beta}_i$  (bounded between 0 and 1) is a weighted average for the first two soil layers (10 and 190 cm deep). For the  $i$ th layer  $\beta_i$  is defined as

$$\beta_i = \frac{\theta_i - \theta_{\text{wilt}}}{\theta_{\text{ic}} - \theta_{\text{wilt}}}, \quad (\text{A4})$$

where  $\theta_{fc}$  is the field capacity (75% of a saturation value of 0.47), and  $\theta_{wilt}$  (=0.1) is the wilting point. Only the portion of the canopy that is dry is allowed to transpire.

#### 4) POTENTIAL EVAPORATION AND POTENTIAL TRANSPIRATION

The MRF model differs from many land-surface schemes (Dickinson 1984; Sellers et al. 1986; Viterbo and Beljaars 1995) in that it first calculates potential evaporation and potential evapotranspiration, which are then used to compute  $E_c$  and  $E_t$  in Eqs. (A2) and (A3), and to set an upper bound on (A1). The potential evaporation is based on a Penman equation [Eq. (5) in Pan 1990]:

$$LE_p = \frac{[(1 - \alpha)S\downarrow + L\downarrow - \sigma T_a^4 - G]\Delta + (1 + \gamma)LE_A}{\Delta + 1 + \gamma}, \quad (\text{A5})$$

where  $S\downarrow, L\downarrow$  are the incoming shortwave and longwave radiation fluxes,  $\alpha$  is the surface albedo (specified at each grid point),  $L$  is the latent heat of evaporation of water,  $\sigma$  is the Stefan–Boltzmann constant (the surface emissivity is 1.0),  $T_a$  is a surface temperature corresponding to the potential temperature of the first model sigma level, and  $G$  is the ground heat flux. The other terms are defined as follows:

$$\gamma = \frac{4\sigma T_a^3}{\rho_a c_p C_h V}, \quad (\text{A6})$$

where  $\rho_a, C_p$  are air density and specific heat,  $C_h$  is a surface transfer coefficient for heat, and  $V$  is the surface wind speed. This term comes from the dependence of the outgoing longwave on  $T_a$ :

$$LE_A = \rho_a L C_h V [q_s(T_a) - q_a], \quad (\text{A7})$$

where  $q_s$  is the saturation mixing ratio, and finally

$$\Delta = \frac{L}{C_p} \frac{dq_s}{dT} \Big|_{T_a}. \quad (\text{A8})$$

When vegetation is present, the MRF model also defines a potential evapotranspiration representing evaporation from a plant with no water stress. This uses a fixed minimum stomatal resistance  $r_s$ , dependent on vegetation type at each grid point (chosen as the annual minimum from Dorman and Sellers 1989) to modify the Penman equation (Monteith 1965), to obtain [Eq. (6) in Pan 1990]:

$$LE_{tp} = \frac{[(1 - \alpha)S\downarrow + L\downarrow - \sigma T_a^4 - G]\Delta + (1 + \gamma)LE_A}{\Delta + (1 + \gamma)(1 + C_h V r_s)}. \quad (\text{A9})$$

Note that  $r_s$  in the reanalysis model has neither seasonal nor diurnal dependence. One consequence is that evapotranspiration is significant in the model at night

if  $LE_A$  is large, for example, in strong winds. It should also be noted that unlike Dickinson (1984) and Sellers et al. (1986), the soil moisture stress term (A4), does not modify  $r_s$  in (A9), but instead directly reduces evapotranspiration in (A3).

Both (A5) and (A9) are derived from energy balance concepts. However, neither of them represents the actual surface energy balance in the MRF model, nor is  $T_a$  the model surface temperature. The model evaporation is calculated from them using (A2) and (A3), and the total evaporation is then an *input* to the model surface energy balance. This energy balance involves the simultaneous solution of the ground heat flux, the model surface temperature  $T_{surf}$ , the longwave radiation field, and the sensible heat transfer to the atmosphere, *given the calculated surface evaporation*. Although this method for calculating the surface energy budget appears to be satisfactory most of the time, we have shown examples in June where the limitations of several model parameterizations combine to give an unsatisfactory surface energy budget.

#### 5) SURFACE FLUX PARAMETERIZATION

The lowest model layer is assumed to be the surface layer ( $\sigma = 0.995$ ) and the Monin–Obukhov similarity profile relationship is applied to obtain the surface stress and sensible and latent heat fluxes. The formulation was based on Miyakoda and Sirutis (1986) and has been modified by P. Long (personal communication) for very stable and very unstable situations. Bulk aerodynamic formulas are used to obtain the fluxes, once the turbulent exchange coefficients have been obtained. The roughness length over ocean is updated with a Charnock formula after the surface stress has been obtained.

##### b. Boundary layer model

There is no explicit boundary layer parameterization in this version of the MRF model. A local stability dependent diffusion scheme is used for the boundary layer as well as the free atmosphere. This scheme follows Louis (1979) and is quite common among global weather and climate models. The coefficient of diffusivity for momentum (subscript  $m$ ) and both heat and moisture (subscript  $h$ ) is expressed in terms of the vertical gradient of the wind as

$$K_{m,h} = l^2 f_{m,h} \text{Ri} \left| \frac{\partial V}{\partial z} \right|, \quad (\text{A10})$$

where the mixing length  $l$  is defined as

$$\frac{1}{l} = \frac{1}{\kappa z} + \frac{1}{\lambda_c}, \quad (\text{A11})$$

$\kappa$  is the von Kármán constant (=0.4), and  $\lambda_c$  is the asymptotic length scale (=250 m). The stability de-

pendence is built into the function  $f(\text{Ri})$  where  $\text{Ri}$  is the local gradient Richardson number. For momentum diffusion, the stability dependence function is given as

$$f_m = \begin{cases} \left[ 1 + 8 \left( \frac{-\text{Ri}}{1 + 1.746 \text{ Ri}^{1/2}} \right) \right], & \text{Ri} < 0 \text{ (unstable)} \\ \left[ \frac{1}{(1 + 5 \text{ Ri})^2} \right], & \text{Ri} \geq 0 \text{ (stable)}. \end{cases} \quad (\text{A12})$$

The corresponding function for temperature and humidity is given as

$$f_h = \begin{cases} \left[ 1 + 8 \left( \frac{-\text{Ri}}{1 + 1.286 \text{ Ri}^{1/2}} \right) \right], & \text{Ri} < 0, \\ f_m, & \text{Ri} \geq 0. \end{cases} \quad (\text{A14})$$

*c. Convection model*

Penetrative convection is simulated following Pan and Wu (1994) based on Arakawa and Schubert (1974), as simplified by Grell (1993). Convection occurs when the cloud work function exceeds a certain threshold. The cloud work function is a function of temperature and moisture in each air column of the model grid point. Cloud mass flux is determined using a quasi-equilibrium assumption based on a threshold cloud work function. The temperature and moisture profiles are adjusted toward the equilibrium cloud function within a specified timescale using the deduced mass flux. The major simplification from the original Arakawa-Schubert scheme is to consider only the deepest cloud and not a spectrum of clouds. The cloud model incorporates a downdraft mechanism as well as the evaporation of precipitation. Entrainment into the updraft and detrainment of the down draft into the subcloud layers are included. The scheme as formulated does not detect low-level inversions, which might inhibit deep convection (see section 4a).

*Acknowledgments.* Alan Betts acknowledges support from the National Science Foundation under Grant ATM-9505018, the National Oceanographic and Atmospheric Administration under Grant NA56GP0380, and NASA under Contract NAS5-32356 for the processing of the FIFE data.

REFERENCES

Arakawa, A., and W. H. Schubert, 1974: Interaction of a cumulus cloud ensemble with the large-scale environment. *J. Atmos. Sci.*, **31**, 674–701.  
 Beljaars, A. C. M., and A. A. M. Holtslag, 1991: Flux parameterization over land surfaces for atmospheric models. *J. Appl. Meteor.*, **30**, 327–341.

Bengtsson, L., and J. Shukla, 1988: Integration of space and in situ observations to study global climate change. *Bull. Amer. Meteor. Soc.*, **69**, 1130–1143.  
 Betts, A. K., 1976: The thermodynamic transformation of the tropical subcloud layer by precipitation and downdrafts. *J. Atmos. Sci.*, **33**, 1008–1020.  
 —, 1984: Boundary layer thermodynamics of a High Plains severe storm. *Mon. Wea. Rev.*, **112**, 2199–2211.  
 —, 1992: FIFE atmospheric boundary layer budget methods. *J. Geophys. Res.*, **97**(D17), 18 523–18 532.  
 —, 1994: Relation between equilibrium evaporation and the saturation pressure budget. *Bound.-Layer Meteor.*, **71**, 235–245.  
 —, and A. C. M. Beljaars, 1993: Estimation of roughness length for heat and momentum from FIFE data. *Atmos. Res.*, **30**, 251–261.  
 —, and J. H. Ball, 1994: Budget analysis of FIFE-1987 sonde data. *J. Geophys. Res.*, **99**(D2), 3655–3666.  
 —, and —, 1995: The FIFE surface diurnal cycle climate. *J. Geophys. Res.*, **100**(D12), 25 679–25 693.  
 —, —, and A. C. M. Beljaars, 1993: Comparison between the land surface response of the European Centre model and the FIFE-1987 data. *Quart. J. Roy. Meteor. Soc.*, **119**, 975–1001.  
 —, S.-Y. Hong, and H.-L. Pan, 1995: Comparison of the NMC/NCAR reanalysis with 1987 FIFE data. NCEP Office Note 410, 83 pp. [Available from NCEP/EMC, 5200 Auth Road, Camp Springs, MD 20746.]  
 —, J. H. Ball, A. C. M. Beljaars, M. J. Miller, and P. Viterbo, 1996: The land-surface-atmosphere interaction: A review based on observational and global modeling perspectives. *J. Geophys. Res.*, **101**(D3), 7209–7225.  
 Chen, F., K. Mitchell, J. Schaake, Y. Xue, H.-L. Pan, V. Koren, Q. Duan, and A. Betts, 1996: Modelling of land-surface evaporation by four schemes and comparison with FIFE observations. *J. Geophys. Res.*, **101**(D3), 7251–7268.  
 Dickinson, R. E., 1984: Modeling evapotranspiration for three-dimensional global climate models. *Climate Processes and Climate Sensitivity*, Geophys. Monogr., No. 29, Amer. Geophys. Union, 58–72.  
 Dorman, H. L., and P. J. Sellers, 1989: A global climatology of albedo, roughness length and stomatal resistance for atmospheric general circulation models as represented by the simple biosphere model (SiB). *J. Appl. Meteor.*, **28**, 833–855.  
 Grell, G. A., 1993: Prognostic evaluation of assumptions used by cumulus parameterizations. *Mon. Wea. Rev.*, **121**, 764–787.  
 Kalnay, E., and R. Jenne, 1991: Summary of the NMC/NCAR reanalysis workshop of April 1991. *Bull. Amer. Meteor. Soc.*, **72**, 1897–1904.  
 —, and Coauthors, 1996: The NCEP/NCAR 40-year reanalysis project. *Bull. Amer. Meteor. Soc.*, **77**, 437–472.  
 Kim, J., and S. B. Verma, 1990: Components of surface energy balance in a temperate grassland ecosystem. *Bound.-Layer Meteor.*, **51**, 401–417.  
 Liang, X., D. P. Lettenmaier, E. F. Wood, and S. J. Burges, 1994: A simple hydrologically based model of land surface water and energy fluxes. *J. Geophys. Res.*, **99**, 14 415–14 428.  
 Louis, J. F., 1979: A parametric model of vertical eddy fluxes in the atmosphere. *Bound.-Layer Meteor.*, **17**, 187–202.  
 Mahrt, L., and H.-L. Pan, 1984: A two layer model of soil hydrology. *Bound.-Layer Meteor.*, **29**, 1–20.  
 Miyakoda, K., and J. Sirutis, 1986: Manual of the E-physics, 87 pp. [Available from Geophysical Fluids Dynamics Laboratory, Princeton University, P.O. Box 308, Princeton, NJ 08542.]  
 Monteith, J. L., 1965: Evaporation and environment. *Symp. Soc. Exp. Biol.*, **XIX**, 205–234.  
 Pan, H.-L., 1990: A simple parameterization of evapotranspiration over land for the NMC medium-range forecast model. *Mon. Wea. Rev.*, **118**, 2500–2512.  
 —, and L. Mahrt, 1987: Interaction between soil hydrology and boundary-layer development. *Bound.-Layer Meteor.*, **38**, 185–202.

- , and W.-S. Wu, 1994: Implementing a mass flux convection parameterization package for the NMC Medium-Range Forecast model. Preprints, *10th Conf. on Numerical Weather Prediction*, Portland, OR, Amer. Meteor. Soc., 96–98.
- Rutter, A. J., K. A. Kershaw, P. C. Robins, and A. J. Morton, 1971: A predictive model of rainfall interception in forests. Part I: Derivation of the model from a plantation of Corsican Pine. *Agric. Meteor.*, **9**, 367–384.
- Schubert, D. D., R. B. Rood, and J. Pfaendtner, 1993: An assimilated dataset for earth science applications. *Bull. Amer. Meteor. Soc.*, **74**, 2331–2342.
- Sellers, P. J., and F. G. Hall, 1992: FIFE in 1992: Results, scientific gains, and future research directions. *J. Geophys. Res.*, **97**(D17), 19 091–19 109.
- , Y. Mintz, Y. C. Sud, and A. Dalcher, 1986: A simple biosphere model (SiB) for use with general circulation models. *J. Atmos. Sci.*, **43**, 505–531.
- , F. G. Hall, G. Asrar, D. E. Strebel, and R. E. Murphy, 1992: An overview of the First International Satellite Land Surface Climatology Project (ISLSCP) Field Experiment (FIFE). *J. Geophys. Res.*, **97**(D17), 18 345–18 371.
- Smith, E. A., and Coauthors, 1992a: Area-averaged surface fluxes and their time-space variability over the FIFE experimental domain. *J. Geophys. Res.*, **97**(D17), 18 599–18 622.
- , W. L. Crosson, and B. D. Tanner, 1992b: Estimation of surface heat and moisture fluxes over a prairie grassland. Part 1: In situ energy budget measurements incorporating a cooled mirror dew point hygrometer. *J. Geophys. Res.*, **97**(D17), 18 557–18 582.
- Strebel, D. E., D. R. Landis, K. F. Huemmrich, and B. W. Meeson, 1994: Collected data of the First ISLSCP Field Experiment. Vol. 1, *Surface Observations and Nonimage Data Sets*, NASA Goddard Space Flight Center, Greenbelt, MD, CD-ROM.
- Sugita, M., and W. Brutsaert, 1990a: Wind velocity measurements in the neutral boundary layer above hilly prairie. *J. Geophys. Res.*, **95**(D6), 7617–7624.
- , and ———, 1990b: How similar are temperature and humidity profiles in the unstable boundary layer? *J. Appl. Meteor.*, **29**, 489–497.
- Viterbo, P., and A. C. M. Beljaars, 1995: An improved land surface parameterization scheme in the ECMWF model and its validation. *J. Climate*, **8**, 2716–2748.